

Two Mars years of clouds detected by the Mars Orbiter Laser Altimeter

Gregory A. Neumann^{1,2}, David E. Smith², and Maria T. Zuber^{1,2}

Abstract. The Mars Orbiter Laser Altimeter (MOLA) instrument operated as an atmospheric lidar system as well as an altimeter, detecting absorptive clouds in northern latitudes shortly after orbit insertion in October, 1997, and reflective clouds over the north polar cap at the start of the Science Phasing Orbits in March, 1998. Global cloud measurements commenced with the primary mapping mission in March, 1999, with nearly continuous coverage for 1.25 Mars years. MOLA tracked several dust storms, culminating with a major dust storm in June, 2001. Reflective clouds, exhibiting distinctive patterns governed by insolation and the dynamics of the atmosphere, were detected at elevations up to 20 km above the surface, chiefly in the polar winter night. MOLA distinguishes cloud returns by pulse width and energy measurements. Unusually strong and brief reflections with minimal extinction suggest precipitation of CO₂ snow under supercooled conditions. Weaker cloud reflections occurred at all latitudes. Some reflective daylight clouds at low latitudes suggested convective vortices or "dust devils". Ground fogs composed of dust and H₂O ice formed at night along the seasonal frost line. Absorptive clouds, while not resolved altimetrically, tracked the advancing and receding edges of the seasonal polar caps. The absorptive and reflective clouds provide a seasonal profile of atmospheric activity spanning two Martian years. Winter reflective cloud activity declined to background levels earlier in the second year at both poles, suggesting interannual warming.

1. Introduction

The Mars Orbiter Laser Altimeter (MOLA) [Zuber *et al.*, 1992; Smith *et al.*, 2001b] is an active remote-sensing instrument, whose primary purpose is to characterize surface topography, roughness, and 1.064 μ m-wavelength albedo. Firing 670 million laser pulses at a rate of 10 per second, MOLA mapped the topography of Mars with > 96% efficiency. Of the non-ground ranges, many were instrumental noise, but nearly 600,000 were spatially and temporally coherent at elevations up to 20 km (Table 1). Thus MOLA measured the distribution of clouds in three dimensions [Zuber *et al.*, 1998]. A sister instrument, the Shuttle Laser Altimeter (SLA) [Bufton *et al.*, 1995; Garvin *et al.*, 1998] had measured cloud returns on Earth, but it was not known prior to the Mars Global Surveyor (MGS) mission whether clouds in the thin Martian atmosphere would be sufficiently dense

to trigger MOLA. Favorable conditions often allowed the detection of abundant clouds, while at other times the altimeter signal was completely absorbed by the Martian atmosphere. Absence of triggers, or unusually low energy return, coincided with significant dust and cloud activity, marking the initiation and progression of atmospheric storms.

Clouds have been observed for more than a century on Mars [Martin *et al.*, 1992], yet their extent, composition and distribution have yet to be fully established. For example, a bluish spring haze surrounding the north polar cap was cited by Percival Lowell as evidence of melting water ice. Daytime hazes are commonly seen in telescopic observations over shield volcanos, and dust storms frequently have obscured surface features. Viking Orbiters observed clouds over several seasons [Kahn, 1984], while recently the Mars Orbiter Camera (MOC) has tracked regional storms and atmospheric hazes [Cantor *et al.*, 2001; Wang and Ingersoll, 2001]. Imaging of atmospheric phenomena is an ongoing component of Mars missions, yet visual observations are limited to daylight.

¹Department of Earth, Atmospheric and Planetary Sciences, Massachusetts Institute of Technology.

²Laboratory for Terrestrial Physics, NASA/Goddard Space Flight Center.

Table 1. Cloud Triggers by Filter Channel and Mission Phase

Channel	Impulse Response ^a	Aerobraking	Mapping	Extended	Total
1	20 ns	6561	84564	2	91127
2	60 ns	4761	88179	7464	1000404
3	180 ns	10333	136524	10159	157016
4	540 ns	14837	204474	14509	233820

^aFull width at half the maximum amplitude

From Viking Lander pressure transducers [Chamberlain *et al.*, 1976] it has been inferred [Hess *et al.*, 1979; Zurek *et al.*, 1992] that a substantial fraction of the CO₂ atmosphere condenses onto the polar regions during seasonal cycles, with observable dynamical and topographic consequences [Smith *et al.*, 1999b, 2001a]. Since daylight temperatures are generally too high for CO₂ frost, much of the condensation takes place in the polar winter night. The mode of condensation, whether surficial or by precipitation from clouds, is unknown.

Although detected by Mariner 6 and 7 [Herr and Pimental, 1970], definitive observations of CO₂ clouds have been lacking prior to MGS [James *et al.*, 1992]. The MGS Thermal Emission Spectrometer (TES) measures daytime atmospheric dust and water ice [Smith *et al.*, 2000, 2001c], but has limited signal-to-noise at low temperatures and thus cannot resolve polar CO₂ ice clouds. Temperatures are consistent with CO₂ ice during polar winter, but the vertical resolution of TES measurements is typically ~ 10 km [Smith *et al.*, 2001c].

The MGS Radio Science (RS) Investigation [Tyler *et al.*, 1992, 2001] determines atmospheric density and temperature at vertical scales of a few hundred meters and sub-Kelvin accuracy by monitoring the frequency of a precise reference radio signal as MGS passes behind Mars. Occultation profiles show that CO₂ condensation may often occur within a few kilometers of the surface during winter months. Radio Science results have further shown that planetary-scale atmospheric waves modulate the temperature and pressure of the polar atmosphere across the CO₂ phase boundary [Hinson and Wilson, 2002].

MOLA is unique in its ability to determine the vertical structure of clouds during the polar winter night [Muhleman and Ivanov, 1998; Zuber *et al.*, 1998; Pettengill and Ford, 2000; Ivanov and Muhleman, 2000a; Ivanov, 2000; Ivanov and Muhleman, 2001], that are invisible to cameras. In daytime, with a higher detection threshold, MOLA sees fewer reflections from clouds, but often sees reduced energy return

from ground pulses. Absence of returns or greatly attenuated energy tracks the presence, but not the altitude, of aerosols and dust in the atmospheric column [Ivanov and Muhleman, 1998]. In section 2 we review the capabilities of MOLA for atmospheric studies and propose a method for distinguishing clouds from noise. Section 3 describes cloud occurrences as a function of season for nearly two years. Section 4 examines their vertical and spatial distribution, and discusses their relation to insolation. Section 5 highlights clouds occurring in low latitudes or in daytime, some related to dust storms. Section 6 looks at contemporaneous profiles of atmospheric temperature from the Radio Science experiment. Finally, in section 7 we examine cloud waveforms and the unusually short pulsewidths of the southern polar clouds.

2. Detection Capabilities of MOLA lidar

The MOLA instrument [Zuber *et al.*, 1992], more sophisticated in its design and operation than the Clementine laser ranger [Nozette *et al.*, 1994] or the NEAR Laser Rangefinder (NLR) [Cole *et al.*, 1997; Zuber *et al.*, 1997], is highly optimized for tracking planetary topography. During mapping, the instrument fires short (~ 8 ns) pulses of laser light in the nadir direction, with a 10-Hz pulse repetition rate that results in ~ 168 -m-diameter footprints spaced roughly 300 m apart during the MGS mapping orbit. The laser shot starts the 100-MHz timing interval unit (TIU), and laser output is recorded. A parabolic mirror focuses reflected photons onto a bore-sighted silicon avalanche photodiode detector. Pre-amplified signals from the detector enter four parallel channels, each with a separate filter and comparator. Channels 1-4 integrate signals using 5-pole Bessel lowpass filters (Table 1), whose time constants correspond to target dispersions of 3, 9, 27, and 81 m. When signal exceeds a software-controlled threshold on any enabled channel, the TIU stops, yielding a round-trip time of flight. Only the first channel to trigger is recorded. MOLA measures the energy and width of pulses using charge-integration circuits from the time of the trigger

until signal drops below the threshold. Twenty records of laser energy, pulse characteristics, and range make up a data "frame". The accuracy of the pulse width and energy measurements after calibration [Abshire *et al.*, 2000] is $\sim 5\%$, although resolution and dynamic range is limited by quantization to a range of 6 and 8 bits, respectively. The majority of energy counts from ground returns are at their maximum value of 255, a condition we call "saturation".

MOLA maintains a histogram of ranges in each 2-s frame [McGarry *et al.*, 1991], setting a range gate to track the ground. The range gate usually excludes returns much higher than 10 km, limiting the height of cloud measurements. Ranges to clouds are latched before ground returns, so that when clouds become dense, MOLA tracks them instead of the ground. When the center of the MOLA range gate tracks a cloud layer for the better part of a MOLA packet (14 s), observation of atmospheric phenomena higher than 10 km is possible. Loss of ranges causes a switch to acquisition mode, whereby range gates are opened to 40 km.

Ground processing determines the position and elevation of each shot with respect to an areoid equipotential surface. Data archived in each daily MOLA Precision Experiment Data Record (PEDR) [Smith *et al.*, 1999a] are classified semi-automatically into ground and non-ground returns using a stochastic tracking algorithm, based on local characteristics of the terrain, followed by manual editing of anomalous points. Pulse width and energy help discriminate ground triggers from noise and clouds. Each frame's PEDR also provides the solar zenith angle Z_s , the local time LT , and the seasonal longitude of the Sun L_s , determined from planetary ephemerides.

Figure 1 shows the laser energy and ranging performance versus L_s for two Mars years of nadir observations. Transmitted energy (crosses) has varied with environmental temperature, declining overall with age, with several rapid fluctuations over periods of a few hours, plausibly due to failures of individual laser diode bars. The fraction of shots (diamonds) that do not trigger at all varies from practically zero to nearly 8%, but performance does not appear to be controlled by the two-fold variation in laser output. Nearly all of the missing triggers, *i.e.*, link failure, result from seasonal atmospheric effects rather than insufficient laser energy.

Non-ground returns (filled squares) are chiefly noise, but increase during polar winters. Instrument noise is limited at night by the characteristics of the detector, and during daytime by scattered incident light. In order to track terrain over a wide range of signal-to-noise ratios, the MOLA flight software sets each channel's detection threshold once per second to maintain a constant rate of background counts. Background normally ranges from 80-160 counts per second, producing approximately 1% false triggers on each channel dur-

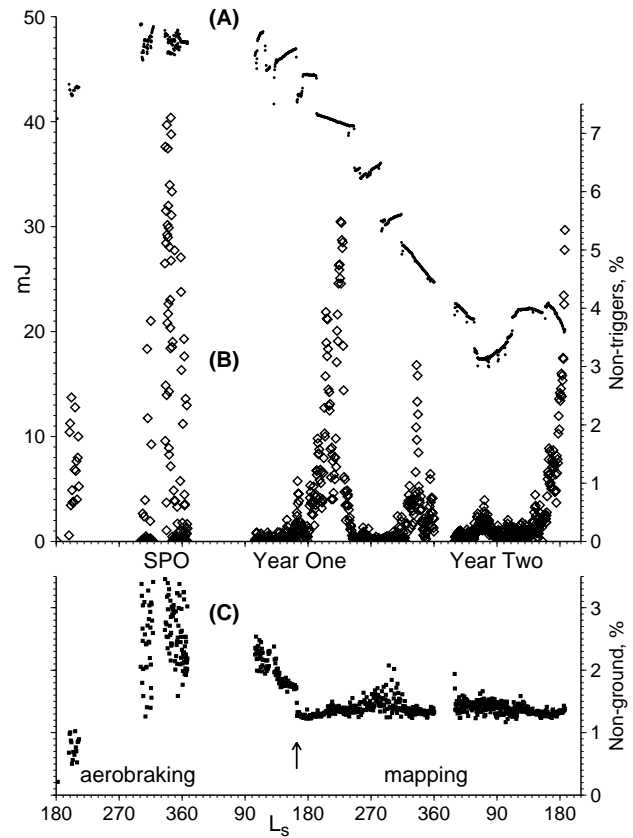


Figure 1. Ranging performance versus seasonal longitude of Sun (L_s), starting at the beginning of northern autumn. Daily averages of (a) laser energy (dots, top, scale on left); (b) missed triggers (diamonds, scale on right) and (c) non-ground triggers (squares). The non-ground returns are due to background noise and reflective clouds. During the aerobraking mission phases (left), observations from elliptical orbits covered the north polar region. After reaching the mapping orbit, observations spanned two martian years (right) with a gap during solar conjunction. The threshold of channel 1 was raised in July 1999 (arrow), reducing noise.

ing the range window. Occasionally the threshold does not respond soon enough and background rises sharply. We exclude from consideration frames with more than 480 background counts per second, or about 3% chance of false triggers in 10 km. In clear skies on flat terrain, channel 1 invariably triggers on ground midway through the range gate, eliminating subsequent noise returns. Starting on July 1, 1999 ($L_s=164^\circ$), the threshold setting of channel 1, normally floating between 45 and 100 mV from night to day, was raised to 245 mV to mitigate the effects of detector saturation. This change eliminated false triggers on channel 1, reducing the rate on all channels from a baseline of 1.7%

early in mapping, to 1.25% (Figure 1c).

The diffuse nature of Martian aerosols limits the rate of cloud triggers (excursions above the baseline in Figure 1c) to a fraction of a percent. The possibility of cloud detection was deemed important enough to provide for a wide range of returning pulse widths with four filter channels. Channel 1 normally triggers first on level ground, as sufficient photons are returned within the equivalent of 3 m range. Channel 4, with the longest time-constant, was designed to trigger on ground slopes of up to 40°, or on cloud fronts. When triggering on clouds, the returning photons are scattered from a layer of roughly 81 m thickness. Intermediate channels respond accordingly. Thus a broad spectrum of cloud types may be detected, and their cross-section measured.

2.1. Link Margins and Absorptive Clouds

Laser output energy, E_{trans} (Figure 1), declined at a slower average rate than had been anticipated, while aging of the detector, optical degradation etc., as measured by a calibration source, have been insignificant. Design margins allowed for the expected decline and still exceeded requirements at the end of the primary mission. The signal in excess of background noise, or link margin, is a function of the received energy, E_{rec} , over a given period of time. This energy is given by the link equation [Abshire et al., 2000]:

$$E_{\text{rec}} = E_{\text{trans}} t_r A_r \frac{r_s}{\pi} \cdot \frac{t_{\text{atm}}^2}{z_{\text{Mars}}^2}, \quad (1)$$

where t_{atm} is the one-way atmospheric transmissivity, t_r is the optical transmission of the receiver, r_s is the surface reflectivity (assuming Lambertian), z_{Mars} is the shot range to Mars, and A_r is the area of the receiving telescope. Detection at night is possible when $E_{\text{rec}} > 20\text{aJ}$ ($20 \times 10^{-18}\text{J}$), equivalent to about 100 photons.

The backscattering cross-section of aerosols per unit time is generally weaker than that of solid surfaces. It was expected (and desired) that the majority of triggers would be from the ground, but the high link margin available to MOLA, relative to the Clementine and NLR lidars, made cloud detection feasible. For example, while MOLA's nominal 45-mJ output is about 1/4 of Clementine's, MOLA's 0.5-m-diameter telescope mirror has a 16-fold larger aperture.

The nominal shot range z_{Mars} is about 400 km in the MGS mapping orbit, varying from 365 to 437 km. During aerobraking, ranges were reliably obtained at nearly twice these distances, indicating a fourfold surplus link at mapping altitude, while over the poles ranges were as low as 170 km, affording even greater margin for detection of clouds.

Equation 1 can be solved for the product $r_s t_{\text{atm}}^2$ of reflectivity and two-way transmissivity, or normalized "return

energy". This product expresses return strength relative to that from a perfectly reflecting Lambertian surface in clear atmosphere. Surface 1.064- μm reflectivity r_s varies seasonally and ranges from 0.09 in the darkest regions to greater than 0.45 over ice [Zuber et al., 1992]. During much of mapping, returns from brighter regions have exceeded the digital range of the pulse energy measurement.

The most dramatic changes in link have been due to changes in Martian atmospheric opacity with season and dust activity. MOLA was designed for an average atmospheric opacity τ of 0.5, or a two-way transmission of 37% [Zuber et al., 1992]. While the Viking 1 and Pathfinder Landers indeed measured such opacities in the late summer [Smith and Lemmon, 1994], the lander elevations are well below the mean equatorial elevation of Mars and thus had a thicker than average atmospheric column. Atmospheric transmission at many surface elevations is higher than average for a large portion of the Martian year. At high elevations, dust opacity is reduced, enhancing link margin for detection of clouds, while during regional dust storms, at the bottom of the deepest canyons and basins, energy returns sometimes fall below detectable levels. Polar hazes with $\tau > 2$ also may prevent MOLA from obtaining range returns.

Figure 2 shows the return energy over the north polar cap during late summer. Detected energy reaches a saturation level over most of the northern lowlands, and only the values below 11% are calibrated. Unusual opacity occurs on both the day and the night side of the cap. None of the non-ground returns, however, are distinguishable from instrument noise, both visually and according to criteria described below. A few of the shots at the night edge of the cap are too weak to trigger at all, where the energy drops below 0.2%. Where the ground is only partially obscured by aerosols, the opacity of the atmosphere may be inferred using an estimate of the surface reflectivity [Ivanov and Muhleman, 2000b].

Reflectivity varies seasonally, and is not accurately known globally. A simple cloud criterion can be based on the returned energy averaged over 20-shot (2-s) data frames. If 3 or more shots fail to trigger on any channel, that is, the returned energy from ground approaches zero, or the average energy is $< 10\%$ of that expected over typical ($r_s = 0.20$) terrain (Figure 2, dashed line), the atmosphere is probably opaque, *i.e.*, $\tau > 1.15$. Such events are termed absorptive clouds.

2.2. Reflective Clouds

Numerous reflective clouds (Figure 3) were detected on orbit 11432, the orbit following Figure 2. These clouds, as with those on two subsequent orbits, lie within a degree of the terminator on the night side of the sunlit north pole.

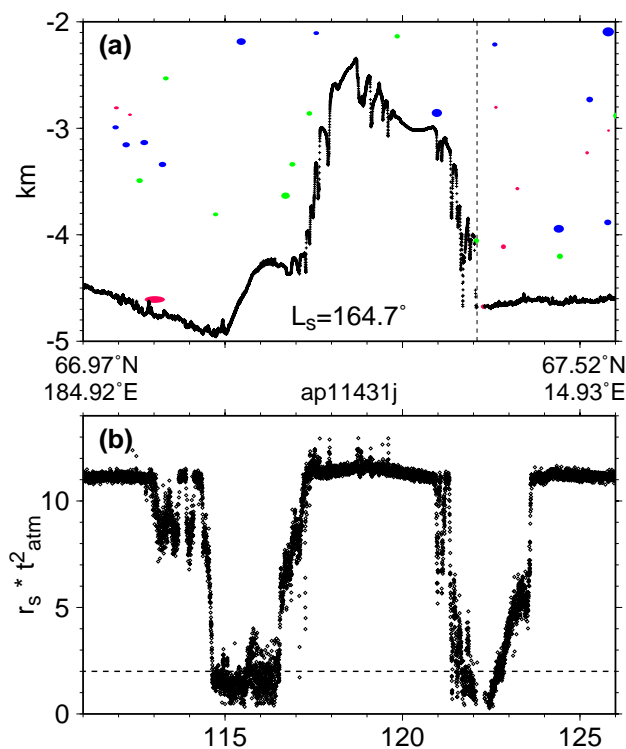


Figure 2. (a) A 15-minute long (~ 2700 km) altimetric profile across Mars' north polar cap, July 4, 1999, at $L_s=164.72^\circ$; the vertical exaggeration is 540:1. Vertical dashed line marks where MGS crosses the solar terminator, from daylight to night. Ground returns are almost all on channel 1 (black), while non-ground returns on channel 2 (red), 3 (green) and 4 (blue) returns are probably instrumental false triggers. (b) The reflectivity-transmission product of ground returns ("return energy") reveals a circumpolar cloud belt. Return energy saturates at $\sim 11\%$. Dropouts and energy values below 2% (dashed line) are termed "absorptive clouds". The horizontal axis on this and subsequent figures is minutes from start of UTC day.

Their appearance was sporadic in late summer, as the atmosphere cooled, and persisted for less than 7 sols. These clouds obscured much of the ground as well. The non-ground triggers occur on primarily on channels 3 and 4, and comprise two low, massive layers. Two scattered triggers, at 0-3 km above datum, exceed threshold for longer than 1400 ns, the maximum digital value recorded by channel 4. Their location indicates a cloud formation extending several km vertically and horizontally. Returns below -2 km are clearly part of a cloud bank, but other returns are not easily classifiable. In particular, channel 2 returns from clouds are seldom much stronger than noise returns in cloudless regions.

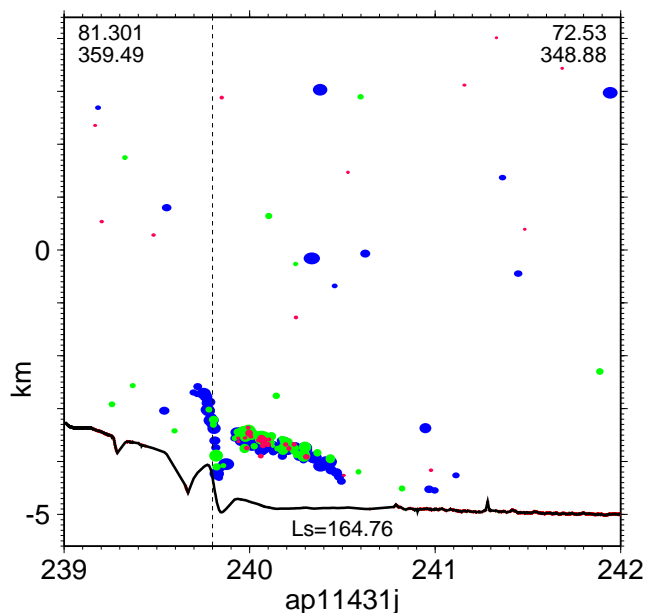


Figure 3. A 3-minute (540-km long) profile showing twilight clouds and noise on MGS orbit 11432, $L_s=164.76^\circ$. The vertical exaggeration is $\sim 50:1$ on this and subsequent figures unless otherwise noted. Vertical dashed line marks the position of the solar terminator. The dark curve shows ground elevation, while 200 non-ground triggers are shown by colored ellipses: channel 2=red, channel 3=green, channel 4=blue. The vertical and horizontal axes of non-ground ellipses are scaled by raw pulse width and energy counts.

Cloud statistics enable us to distinguish reflective clouds from noise with reasonable confidence. Reflective clouds, as opposed to hazes, often occur in clusters [Ivanov and Muhleman, 2001]. Most non-ground triggers result from noise, and such noise is uniformly distributed in time, so that multiple noise events within a short interval of time are unlikely to occur.

The probability of exactly n false triggers in a 6-s window of time is given by a binomial distribution:

$$P_n^m = \binom{m}{n} P_{fa}^n (1 - P_{fa})^{m-n}, \quad (2)$$

where $m \leq 60$, since some triggers are skipped for operational reasons. The distribution for $P_{fa} = 1.25\%$ fits the observed histogram during clear conditions (Figure 4).

For each above-ground trigger, if 5 or more additional triggers in the preceding and following 3-second window of time are non-ground, such a detection is presumed to be a portion of a cloud. Such a criterion is optimum for clouds of roughly 18 km extent. While longer windows of time might discriminate clouds with greater confidence, many clouds

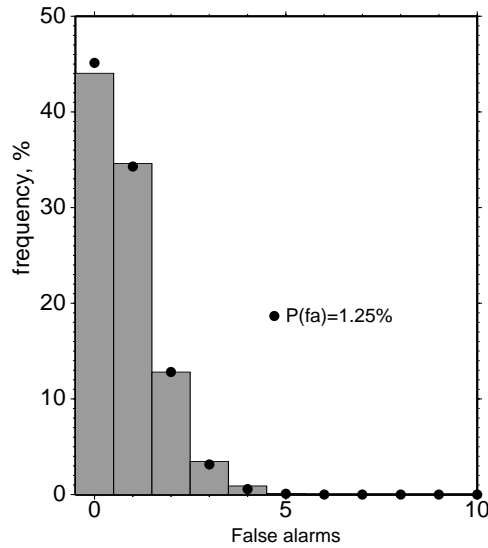


Figure 4. The number of false-triggers obtained by MOLA in clear atmosphere over a six-second period fits a binomial distribution (dots) with $P_{fa} = 0.0125$. The likelihood of six or more false triggers is <1 in 10^5 .

occur in short bursts and might be excluded. The probability of such a large number of noise triggers is $\sum_{n=6}^m P_n^m$, and is <1 in 10^5 . We also interpret the trigger as a cloud if 2 or more triggers in any of the 2 preceding and following shots are non-ground, since the probability of this occurring by chance is also <1 in 10^5 . In Figure 3, there are several probable cloud returns near 241 minutes, but these are not close enough in time to be distinguished from noise. Moreover, the vertical dispersion of clouds is usually large. We do not use vertical correlation as a means of classification. Any classification scheme is subject to error, but our criterion identifies the majority of clouds with minimal false returns.

Plate 1 shows the fraction of returns produced by clouds within a given $2^\circ \times 2^\circ$ bin in latitude and solar longitude, as a quasi-logarithmic color density plot, from $L_s=104^\circ - 360^\circ$ and $L_s=29^\circ - 187^\circ$, denoted mapping Year 1 and Year 2. The number of clouds in the ~ 46 passes through a given time-latitude bin is normalized by the number of MOLA shots in the bin. Temporal variation at shorter intervals may be present, but daily sampling is too sparse to resolve it. The resulting cloud density is divided by the average laser output (Figure 1) relative to a nominal 25 mJ, to remove some of the observational bias due to differences in link margin over the course of the MGS mission. Clouds associated with the winter polar caps dominate the observations, and can reach densities higher than 10%. Most of the clouds lie within the region of polar winter darkness, denoted by the latitude at

which MOLA profiles cross the terminator. Less frequent atmospheric disturbances occur in the circumpolar regions and at mid-latitudes. The density of clouds in mid-latitude bins is extremely low, and where $<0.005\%$ they are not assigned a color. Many of these clouds are simply correlated noise returns, a function solely of instrument threshold. A change in threshold early in the mission (arrow) reduces noise, while as laser output declines, normalization appears to increase their density.

3. Chronology

3.1. Reflective cloud history

The MGS aerobraking mission phase and the mapping mission phase entailed distinct geometries and seasonal coverage. MGS entered an eccentric, two-day-period orbit on September 13, 1997, shortly after the start of northern autumn, $L_s=181^\circ$. On September 15 (contingency science pass 3), MOLA was programmed to range from its hardware limit of 786 km down to periapsis and back, returning 21 minutes of data with nearly 100% ground detection. MOLA opportunities were limited to brief periapse passes until the 40,000-km apoapsis could be lowered by aerobraking. During these 121-km-high maneuvers, the instrument deck was tilted away from nadir. The mission originally planned to achieve a near-circular, near-polar, 400-km mapping orbit by early 1998. Aerobraking caused undue flexure of a solar panel and was halted in October after 18 orbits by raising periapsis height to 170 km. The revised plan entailed slower aerobraking but allowed some nadir-pointing science activities before mapping. These were the aerobraking assessment passes 20-36 ("Hiatus"), and the Science Phasing Orbits 203-268 and 318-457 (SPO-1 and SPO-2, corresponding respectively to periods before and after solar conjunction), during which aerobraking was suspended to allow the MGS orbit plane to reach the desired 2 PM/2 AM local solar time.

Reflective clouds were not identified on pass 3, nor during the Hiatus passes at $L_s=192-213^\circ$, in the early northern autumn. Ground tracks within MOLA's range commenced at roughly 78°N , in local dusk, ending near the equator. If reflective clouds were present during Hiatus, they might have been detected near the extreme limit of range (*cf.* Plate 1), but their presence was unlikely due to the late afternoon local time. Reflective clouds were observed one Martian year later only at higher latitudes, as seen in Plate 1.

Attenuation or extinction of laser pulses was observed on several days during Hiatus between 60 and 75° latitude. *Ivanov and Muhleman* [1998] and *Hansen* [1999] ascribed these opacity events to the polar vortex circulation, tentatively identifying them as water ice hazes. After repeated signal losses, MOLA enters acquisition mode, reinitializing

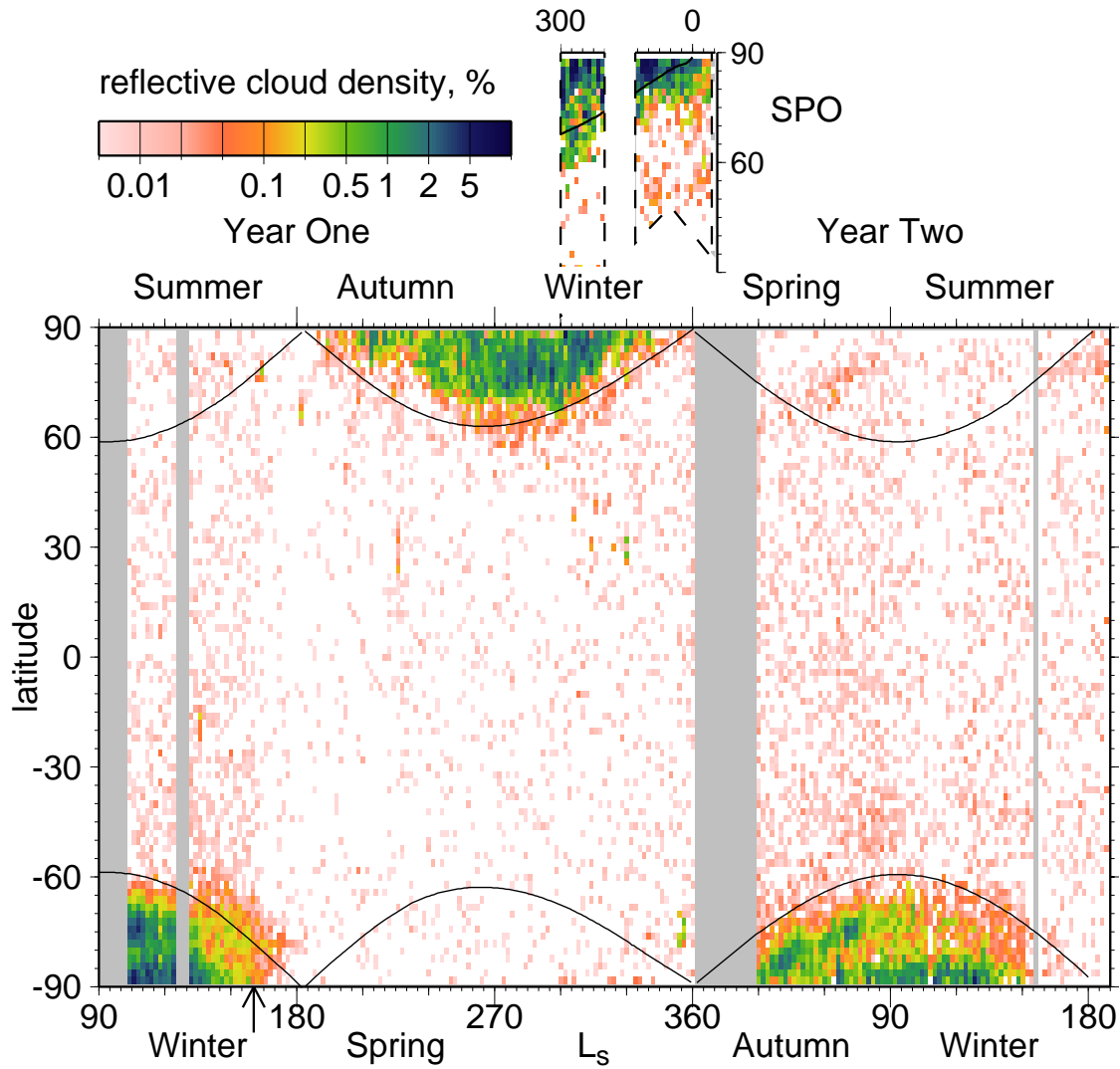


Plate 1. Percentage of reflective cloud counts in $2^\circ \times 2^\circ$ bins, as a function of the solar longitude L_s and latitude. The cloud frequency as a fraction of nadir-looking shots is normalized by laser energy. The nearly constant rate of false returns thereby appears to increase as the laser energy declines during Year Two. The inset shows the limited extent of coverage during the Science Phasing Orbits (SPO). The curves show latitude of the terminator along the MOLA ground track, offset from the arctic circles due to the ~ 2 pm sun-synchronous orbit. The arrow shows the time at which threshold of channel 1 was raised to mitigate saturation of ground returns; the background resulting from false triggers was thereby reduced.

its detection thresholds at a very low setting, with a corresponding increase in background noise counts. Such high background causes MOLA to trigger shortly after opening its range window, generating clustered false returns that resemble clouds. After 1 s, the acquisition algorithm raises the detection threshold. Triggers in acquisition mode are excluded from the present analysis. The reflective clouds reported by Hansen [1999] subsequent to loss of signal were artifacts of a lowered threshold.

Aerobraking recommenced in November, 1997. MOLA was turned on intermittently starting March 1998, the beginning of SPO-1. During SPO, the MGS periapsis conveniently precessed over the north pole. MGS altitudes as low as 170 km provided very high link margins, and clouds appeared daily. All four channels detected clouds.

Observations of reflective clouds [Zuber *et al.*, 1998; Pettingill and Ford, 2000] began at $L_s=305^\circ$, on Pass 203. The inset on Plate 1 shows cloud density in the 1998 late

northern winter season. The aerobraking phase orbits covered the northern hemisphere every 11h 37m. During this phase, MOLA obtained nearly 26 minutes of observations on each pass. Most clouds were poleward of 75°N. Few (if any) clouds were seen at latitudes below 60°S.

After a 4-week pause for solar conjunction in May, observations resumed at $L_s=335^\circ$ during SPO-2. Clouds receded poleward until the end of science phasing observations in early northern spring, $L_s=7^\circ$. MOLA remained off from August 1998 to February, 1999, except for a successful Phobos flyby in September [Banerdt and Neumann, 1999; Smith *et al.*, 2001b].

MGS attained mapping orbit at the end of February, 1999, at $L_s=103^\circ$. At that time, reflective clouds were prominent high over the southern pole. Cloud activity peaked at $L_s=110^\circ$ and was seen as far north as 55°S, shortly after the start of austral winter. After a month-long check-out and gravity mapping campaign, the MGS high-gain antenna (HGA) was deployed to its articulating position to allow full-time mapping and radio tracking. Operations were interrupted at $L_s=126^\circ$ for two weeks to resolve problems with the antenna gimbal stops, following which reflective clouds were observed in the south until the vernal equinox at $L_s=180^\circ$. South polar clouds formed two semi-distinct regions, one over the pole and a band surrounding the cap at 68-79°S [Ivanov and Muhleman, 2001]. Until the threshold of channel 1 was raised, returns from channel 1 made up the majority in the circumpolar band.

Sporadic reflective clouds were detected over the north polar cap in summer from $L_s=145^\circ$ to 180° at 75°-80°N (Figure 3). These migrated southward during northern autumn, coinciding with increasing dust storm activity. North polar clouds did not appear persistently until $L_s = 194^\circ$, extending southward of 75°N by $L_s = 240^\circ$. By $L_s=280^\circ$, reflective clouds had peaked in density, extending southward to 55°N. Clouds had vanished by the onset of northern spring. The north polar clouds during Year 1 of mapping appear to have ended earlier than at the corresponding time in SPO. One must consider observational bias due to the rapidly varying ranges, the distinctly different local times, and somewhat higher laser output during SPO. Nevertheless, northern clouds had declined to near-background levels in Year 1 by $L_s = 345^\circ$, suggesting an end at least 20° earlier than SPO [Ivanov and Muhleman, 2001]. As north polar clouds waned, sporadic groups of clouds commenced at $L_s = 300^\circ$ and 40°N, coincident with recession of the seasonal cap. Similar, sparse cloud formations were observed during the corresponding period in SPO (inset).

Clouds reappeared in the southern hemisphere for a few days at $L_s = 352^\circ$, at latitudes of 70°-80°S. MOLA was turned off on June 1, 2000 for solar conjunction, shortly af-

ter $L_s=360^\circ$, and resumed operation on Aug. 1 at $L_s=30^\circ$. At this time clouds extended diffusely over the southern pole to 75°S. As was the case the previous year, two semi-distinct regions of polar and off-polar clouds formed. Observations continued through the January 2001 end of the MGS Primary Mission, and into the Extended Mission. Reflective clouds over the south polar cap were waning at $L_s=154^\circ$ when operations were interrupted by a spacecraft anomaly on May 2. After restarting a week later, MOLA saw few southern clouds.

Plate 1 shows that cloud detections ended considerably earlier during Year 2 than during Year 1. Fewer clouds might be expected in Year 2, owing to a higher channel 1 threshold and a nearly 50% decline in laser energy. Only 1/3 as many clouds were seen during the second southern winter, but very few south polar clouds were seen after $L_s=150^\circ$, while Year 1 had appreciable cloud returns until $L_s=166^\circ$. Hundreds of clouds in Year 1 were saturated in energy after $L_s=150^\circ$, dozens even after $L_s=180^\circ$. These saturated clouds should have been seen in Year 2 despite laser aging. Only two such clouds occurred in Year 2 after $L_s=150^\circ$, while in the previous month, saturated clouds were seen daily. These observations suggest that south polar clouds ended sooner in Year 2.

After nearly 4 years of operation, MOLA experienced a loss of ranges during the Extended Mission on June 30, 2001 at 11:10:40 UTC ($L_s=187^\circ$). MOLA was shut off a few hours later as laser temperature fell below operating limits. The anomaly was traced to the loss of the 100-MHz timing oscillator signal. All other systems remained healthy, and MOLA continues to operate as a narrow-band radiometer [Sun *et al.*, 2001].

3.2. Absorptive Clouds

Non-reflective or absorptive clouds occur both day and night with nearly equal frequency. These clouds or hazes (Figure 2) are distributed widely (typically extending over hundreds of kilometers), are often visible in images, but seldom return sufficient photons within a given interval of time to trigger. Even with initially high laser output, they attenuated ground returns to extinction, implying opacity >2 . Opacity events resulted in loss of signal for many seconds during passes 21, 24, 30, and 35 in Hiatus without reflective clouds (see previous section). Extinctions in SPO-1 were generally associated with reflective cloud activity, while during SPO-2, were often due to circumpolar, absorptive clouds.

Plate 2 shows the percentage of nadir-looking frames with absorptive clouds as a function of season and latitude. Opacity peaked during northern autumn, at latitudes from 55°N to 85°N, coincident with local dust storms. Opacity events were concentrated in the boreal lowlands, as well as

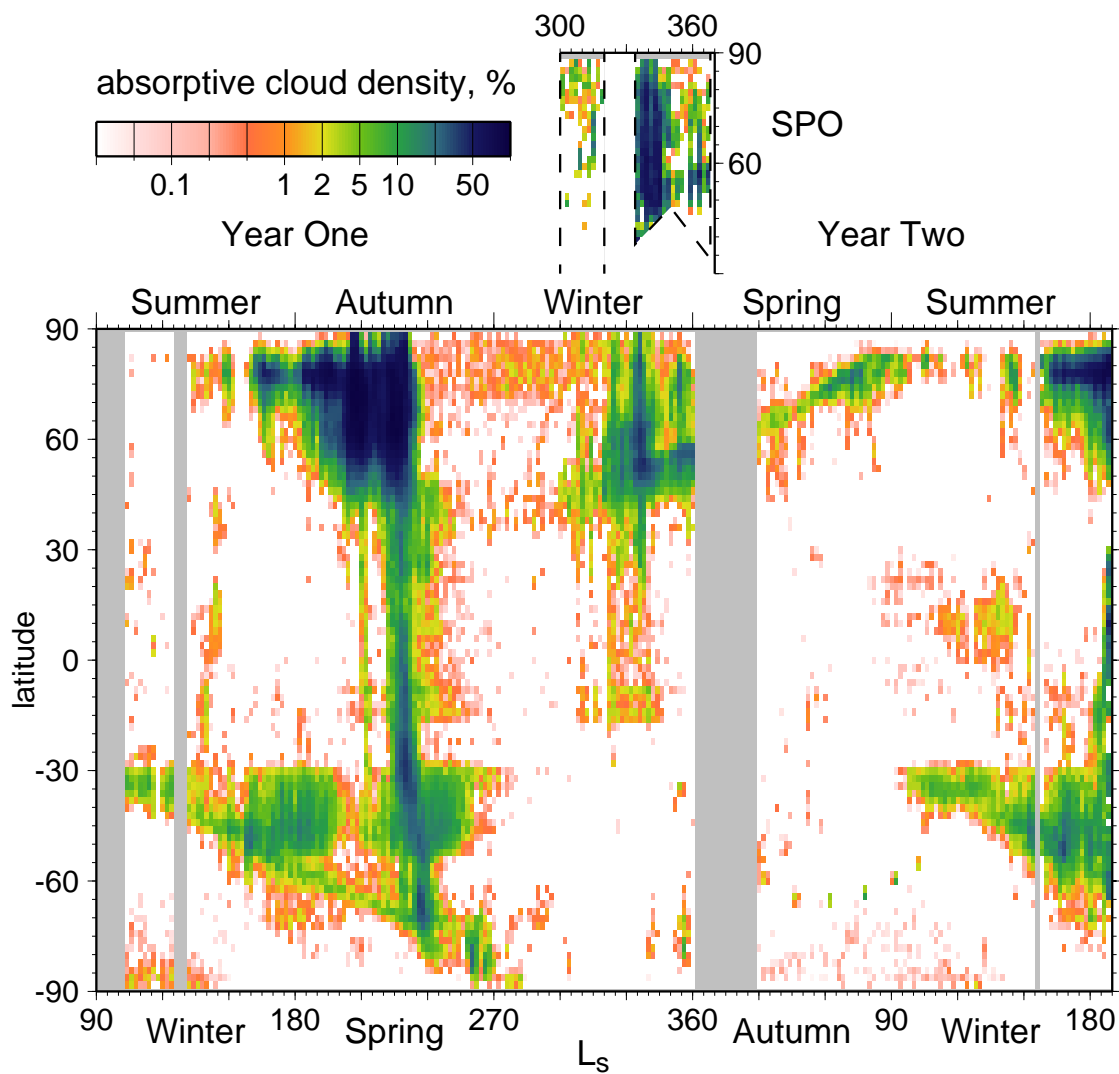


Plate 2. Frequency of absorptive clouds with latitude and season. Nadir frames with average reflectivity-transmission product < 0.02 , or more than 2 shots that return no ranges, indicate significant opacity. The percentage of frames in bins of 2° by 2° in L_s and latitude is colored in a quasi-logarithmic scale.

latitudes from 30°S to 50°S in the 8-km-deep Hellas Basin.

Early in mapping, dust storms were evident in MOC images and TES spectra [Kieffer *et al.*, 2000; Pearl *et al.*, 2001; Smith *et al.*, 2001c]. Clouds in the northern hemisphere began to obscure the ground in mid summer, ($L_s=145^\circ$), with the onset of near-global occlusion at $L_s=210^\circ$, followed by an even stronger episode at $L_s=225^\circ$. The first episode commenced in the north polar lowlands. Atmospheric dust in the southern hemisphere rapidly became apparent in Hellas. A later episode occurred over Sinai Planum in the southern hemisphere, obscuring the floors of both Hellas and Argyre. By $L_s=230^\circ$ dust storms in the southern hemisphere

obscured the floor of Valles Marineris. Reflective clouds were sometimes seen during this opacity event in the northern hemisphere but seldom in the south. Clearing occurred rapidly at $L_s=245^\circ$. Higher-than-normal opacity continued over the northern polar cap, but the bulk of the polar winter night remained free of absorptive clouds.

Renewed activity appears after $L_s=300^\circ$, commencing at 35°N , building to regional storms in the next two months until Spring. Following a gap of coverage at solar conjunction in June-July 2000 from $L_s=2^\circ-30^\circ$, a narrow opacity belt migrates steadily northward almost to the pole by $L_s=98^\circ$, in December 2000. This belt terminates just after the sum-

mer solstice at the $\sim 80^\circ\text{N}$ latitude of the permanent polar cap. Reflective clouds were occasionally seen along this belt (Plate 1).

A southern opacity belt commences shortly after winter solstice at 30°S , $L_s=100^\circ$, along with persistent clouds in the Hellas and Argyre basins. This narrow zone migrated slowly southward to the antarctic circle at $L_s=210^\circ$, accelerating toward the pole at $L_s=250^\circ$, reaching it just after the summer solstice. Poleward of the belt the atmosphere was relatively transparent, and remained so after $L_s=270^\circ$. The cloud belt is closely associated with the sublimation of the seasonal frost layer as observed by TES [Kieffer *et al.*, 2000] and MOC [James *et al.*, 2001]. Minimal opacity was associated with the advance of the southern seasonal cap in late summer and fall of Year 1, with nearly identical behavior in the second year of mapping. Opacity rose in both hemispheres during May and June 2001, culminating in a global dust storm lasting several months. Ranging was impaired from $L_s=160^\circ$ to the cessation of operation (Figure 1).

MOLA cannot determine the composition of absorptive clouds, since their height and density profile are unknown, but we will argue in section 5 below that reflective clouds have distinctive compositions. We remark that atmospheric H_2O [Smith *et al.*, 2001c] increases in the northern hemisphere from spring to mid-summer, so water ice may have contributed to absorption. In mid- to late northern summer during both mapping years, opacity develops west of Tharsis and Elysium from the equator to $\sim 40^\circ\text{N}$, but without associated reflective clouds. This opacity is related to the increased water ice in the northern hemisphere at this time [Tamppari *et al.*, 2000; Pearl *et al.*, 2001]. Such clouds only rarely obscure the surface but are clearly seen in the calibrated energy return [Ivanov and Muhleman, 1998].

4. Cloud Distribution

4.1. Geographic

Absorptive clouds are topographically and seasonally controlled. Owing to a thicker atmospheric column, the ~ 8 -km-deep Hellas and Argyre basins nearly always exhibited some attenuation of pulses. Strong absorption occurs frequently over the northern lowlands and in the Valles Marineris, suggesting attenuation by vertically mixed aerosols [Ivanov and Muhleman, 1998]. The criterion we have employed highlights absorptive clouds over the darker regions, including the Argyre-Chryse trough and Syrtis Major, while masking those over the brighter Tharsis, Arabia, and Elysium highlands. Nevertheless, the aphelion water ice clouds [Smith *et al.*, 2001c] over Olympus and Tharsis Montes reach sufficient density to obscure the ground. A fully calibrated opacity survey using both active and passive MOLA radiometry

[Sun *et al.*, 2001; Ivanov *et al.*, 2001] will clarify their distribution further.

Reflective clouds are primarily latitudinally controlled, with some longitudinal variation. In particular, reflective clouds with very short pulse widths and returns exclusively on channel 1, termed "channel 1 clouds", appeared frequently in the southern hemisphere poleward of 65°S . Clusters of channel 1 returns were observed during SPO poleward of 75°N , but always intermingled with channels 2-4. Latitudes between 76°S and 82°S have fewer than average clouds, as seen in Figure 5. While clouds may be associated with topographic features such as crater rims, or form low fogs in crater interiors, surface elevation does not strongly control reflective cloud distribution in either hemisphere. The highest densities occurred over the polar residual ice caps and surrounding layered terrain in both hemispheres (Figure 5).

In the north, clouds were fairly common over the entire boreal basin, extending to lowest latitudes into Acidalia Planitia at $\sim 315^\circ$ - 355°E . Several very cloudy days dominate the observations in the 0° - 180° hemisphere. Substantial gaps occur over part of Olympia Planitia and in the Chasma Boreale region. The pattern is complex and not obviously associated with major topographic features, although Ivanov and Muhleman [2001] suggests they are triggered by higher km-scale roughness.

In the south, higher densities occurred over the Mountains of Mitchel and the southern edges of Argyre and Hellas Basins. There is a preference for longitudes along a 150° - 330° axis, offset toward 330° from the pole. Temperature profiles obtained by Radio Science in southern winter [Hinson and Wilson, 2002] at 67 - 70°S from $L_s=134^\circ$ - 148° reveal planetary-scale waves with significant amplitudes at zonal wavenumbers 1 and 2. Phasing of these weather systems yields a temperature minimum near 330° E longitude. Such structure is consistent with the offset of the cloud density in the direction of the highest elevation of the polar cap. Some clouds appear to be tied to atmospheric circulation [P.G. Ford and G.H. Pettengill, personal communication, 2000], with correlation of clouds seen on consecutive passes suggesting an eastward longitudinal drift.

4.2. Vertical

Figure 6 compares the vertical distribution of reflective clouds from north to south. Northern winter clouds are densest at 6-8 km above the surface, and may reach altitudes of 20 km. Southern clouds are seen most often at 1-3 km height, and seldom exceed 15 km. Because of the roughly 6-km difference in elevation of the polar caps, the clouds appear at roughly the same geopotential heights, the median being about 2.3 km in the north and 4.3 km in the south. In

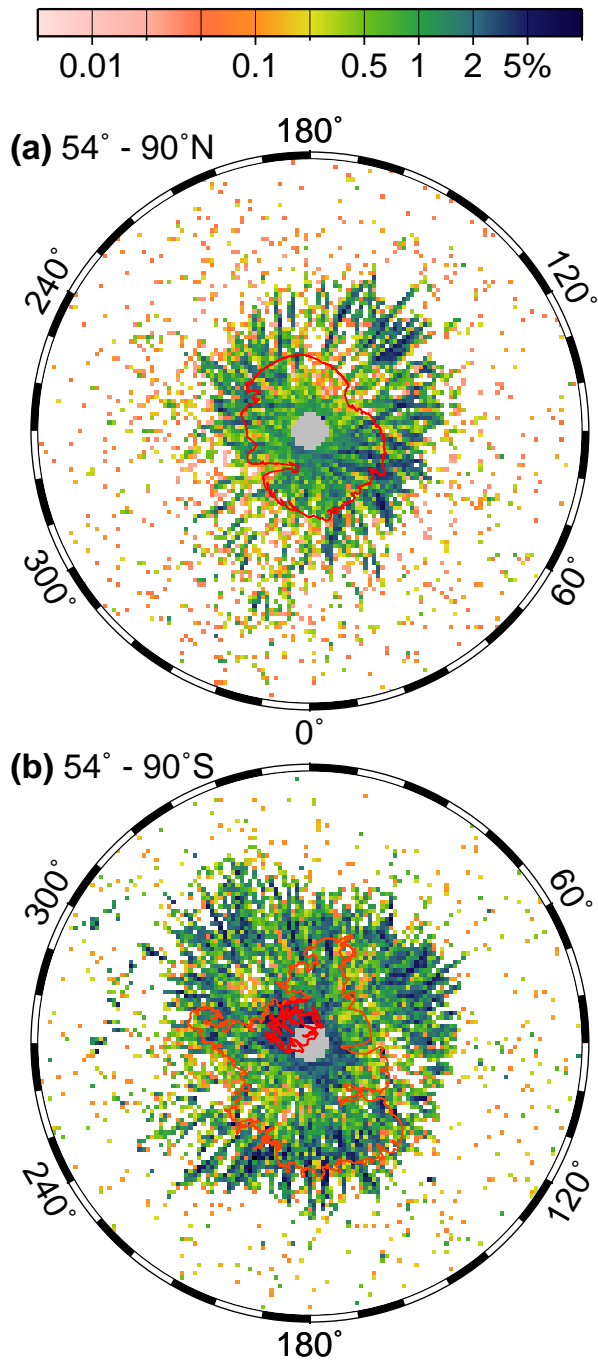


Figure 5. Reflective cloud distribution of (a) north pole during $L_s=180^\circ$ to 360° of Year 1, and (b) south pole during $L_s=104^\circ$ to 180° . The density of occurrences is normalized by range observations. The contours denote the extent of permanent polar ice and south polar layered terrains. The projection is polar stereographic to 54°N/S .

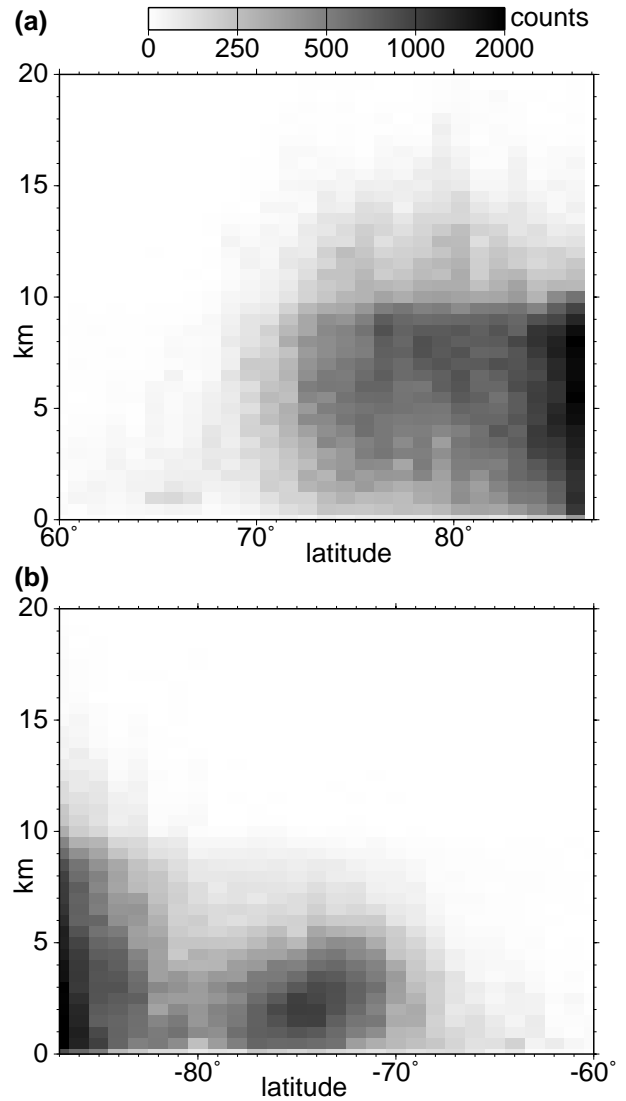


Figure 6. Latitude-height distribution of polar clouds during MGS mapping Year 1, $L_s=104^\circ$ to 360° . The instrument’s usual range gate setting results in an artificial dropoff in cloud density at 10 km height.

particular, few clouds are situated close to the ground in the northern lowlands from 70° - 80°N , while near the polar cap, cloud fronts sloping at angles $> 30^\circ$ toward the ground were fairly common. These observations suggest that atmospheric pressure, rather than a surface boundary layer, controls vertical cloud density.

South polar clouds form a belt around the cap, separate from and lower than clouds over the cap. The circumpolar clouds are concentrated within 5 km of the ground. During Year 1, the majority were seen on channel 1 (Figure 7), while

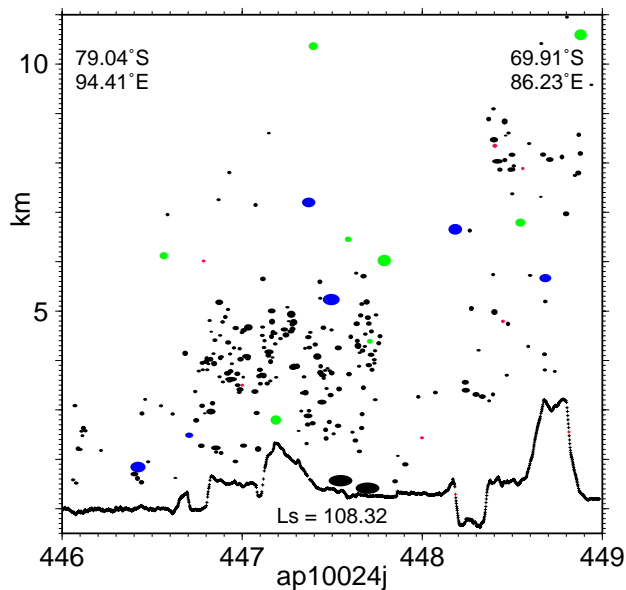


Figure 7. Circumpolar belt of channel 1 clouds observed on March 11, 1999. In this profile segment nearly 1/3 of MOLA shots trigger on clouds. Two unusually strong channel 1 returns occur at 160-200 m above ground.

in Year 2, with higher channel 1 threshold settings, mainly on channel 2 but occasionally on channel 1. The channel 1 clouds were seen exclusively at night, ranged widely in elevation, and exhibited little structure. No attenuation of ground returns between clouds is observed. The received energy was usually much lower than for ground returns, with the mode being about 40 aJ. Figure 8 shows an example of both narrow pulse return and extended return clouds, separate in location and elevation.

4.3. Solar Zenith Angle

Figure 9 shows the occurrence and frequency of reflective clouds vs. solar zenith angle. Reflective clouds are mainly seen at night, that is, where solar zenith is greater than 90° . Fewer clouds occur in twilight, and very few below 80° where sunlight penetrates nearly everywhere. While the higher threshold required to exclude solar background masks daytime reflections from dust and ice hazes, a significant number of such triggers occurred during the dust storm event at $L_s=230^\circ$. Daytime clouds are evident in the northern summer at latitudes $> 65^\circ$, forming a band that recedes to the permanent polar cap as summer approaches, remaining until $L_s=160^\circ$. Most of these clouds correspond to opacity events.

Southern clouds are virtually absent during the summer daytime, with the elevated temperatures close to perihelion.

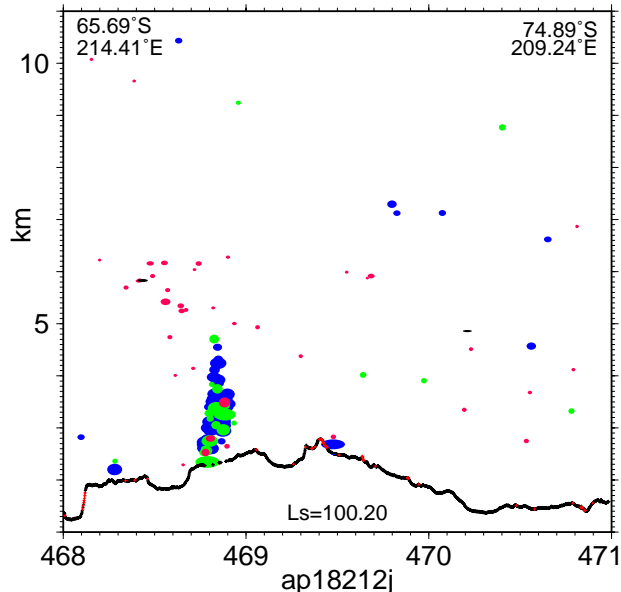


Figure 8. Circumpolar clouds seen on January 8, 2001 during Year 2. Laser output is lower, and channel 1 threshold is too high to trigger on clouds, but channel 2 clouds are seen.

lion. Almost all southern reflective clouds with zenith angles $< 90^\circ$ are winter clouds, very close to the terminator, and not associated with high opacity. Many craters show clouds closely associated with their rims, extending into twilight.

Clouds observed equatorward of 50° latitude comprise about 3% of the total number of reflective clouds. Equatorial (-50° to 50° latitude) daytime clouds are almost as numerous as nighttime equatorial clouds, and appear to be related to dust or opacity events, as we describe in the next section.

5. Non-polar-winter Clouds

Reflective clouds sometimes occur along the edges of the seasonal caps, before and after the formation of the polar cloud belts. The earliest autumn north and south polar clouds are isolated in temporal and spatial occurrence from the main polar autumnal and winter cloud formations. All of these clouds occur within a few hundred meters of the ground and appear on the night side, after midnight local time. During spring and summer, after the polar clouds have vanished, such clouds will occasionally be illuminated in polar evening twilight (Figure 10).

Spring/summer clouds are usually dense and opaque, often blocking the ground completely, and are surrounded by regions of very weak ground returns. Clouds lying within a few hundred meters of ground are also seen in the polar winter night, but these occur when the atmosphere is rela-

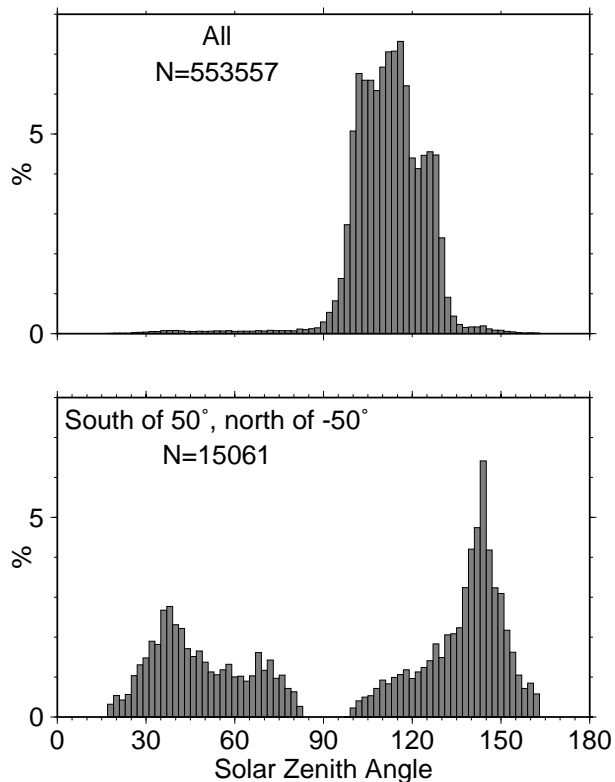


Figure 9. Histograms of reflective clouds vs. solar zenith angle. Most clouds occur at night or twilight. Equatorial clouds are almost equally distributed day and night.

tively transparent and all surrounding shots have maximum recorded pulse energies. Optically dense night fogs are not limited to polar regions, but may occur close to the ground at mid-latitudes. Particularly bright and dense groups of low clouds occurred on May 10 and June 7, 1999 at 18°-25°S in late southern winter ($L_s=136^\circ$ and 151°). Such mid-latitude fogs are closely associated with atmospheric disturbances producing absorptive clouds and lower energy returns, but are not seen during the times of heaviest absorptive cloud cover. If these night fogs were simply dust, they should appear during daylight as well, given that diffuse dust clouds are seen during daylight (see below) and the energy return of these fogs is high. The occasional nocturnal visibility of these low reflective clouds suggests "bright" condensates onto darker dust. Mid- to equatorial-latitude temperatures in the lower atmosphere are generally too high for dry ice crystals to form, but at 190-200 K, lie below the frost point of water ice. Low ground fogs, made reflective by water ice, corroborate the inference from Mars Pathfinder Imager that water vapor is concentrated within a near-surface boundary layer [Titov *et al.*, 1999].

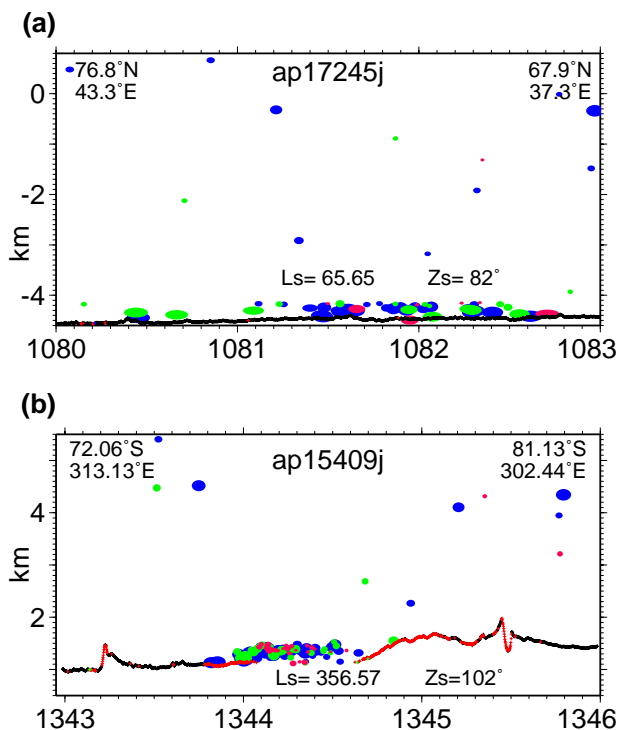


Figure 10. (a) Late Spring fog in Northern polar twilight. (b) Late Summer fog in Southern polar night. Both occur shortly after midnight local time.

Many low-latitude daylight clouds form narrow pillars (Figure 11), with vertical extent of up to 10 km over a distance of 5-10 km. These clouds often coincide with absorption of ground returns. They are widely distributed over the plains and preceded the major dust storm of 2001 observed by TES at $L_s=170^\circ$ [Smith *et al.*, 2001c]. Their diffuse, vertical nature, and corroborating observations [Cantor *et al.*, 2001] suggest that some of these are "dust devils", convective vortices that entrain and lift dust from the surface, while others appear to be orographic clouds. Table 2 gives the times of several such events. The height of these features is 5-10 km, consistent with the finding that a convective boundary layer extends to an altitude of 8-10 km during summer [Hinson *et al.*, 1999].

Other probable dust-storm-related clouds are seen in the deeper regions of Valles Marineris, Argyre and Hellas. These are very diffuse and seldom occur in sufficient numbers within 6-s (18 km) intervals to be identified statistically. Dust and haze are more often apparent in Hellas by their weakened ground returns through thick atmospheric columns. Regions of absorptive clouds frequently appear at 30°-50°S (Plate 2).

Table 2. Selected Cloud Pillars Observed by MOLA

Orbit ^a	L_s	Ephemeris Time	latitude	longitude	Z_s	LT ^b	height
18848	124.14	2001 MAR 01 10:31:27	53.08	138.18	41.33	14.18	7 km
19166	136.67	2001 MAR 27 10:33:00	39.41	29.73	38.16	14.34	9 km
19190	137.80	2001 MAR 29 17:33:51	49.64	305.51	43.2	14.27	8 km
19215	138.56	2001 MAR 31 06:49:18	43.24	122.33	40.26	14.33	10 km
19300	142.05	2001 APR 07 07:09:08	-41.9	190.25	67.8	14.69	9 km
19300	142.34	2001 APR 07 21:12:16	15.11	341.77	35.8	14.48	8 km
19533	151.84	2001 APR 26 14:20:30	-48.6	269.1	70.43	14.81	8 km

^aOrbit = 10000+mapping orbit number at start of calendar day

^bLocal time as decimal hours of 24 in a Martian sol.

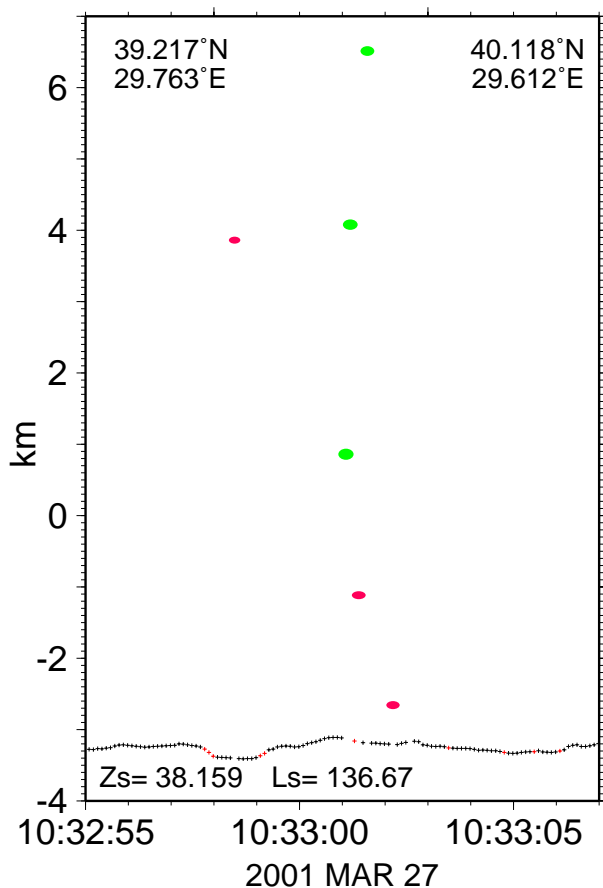


Figure 11. Daytime cloud, probably dust entrained in a convective vortex, or "dust devil", in PEDR ap19166j.b. The vertical exaggeration is 5:1.

6. Clouds and Temperature Profiles from Radio Science Investigation

The Martian atmosphere perturbs radio signals as spacecraft pass behind the planet [e.g., Lindal *et al.*, 1979]. The MGS Radio Science Team has archived > 3700 occultations during the primary mission [Tyler *et al.*, 2001], providing atmospheric temperature-pressure profiles with sub-Kelvin accuracy and vertical resolution better than 1 km. Favorable MGS-Earth geometry provided many occultations at polar latitudes in 1999 and again in 2000 [Hinson *et al.*, 1999, 2001; Hinson and Wilson, 2002]. The location on Mars where the signal ray path grazes the planetary surface is, however, remote from the MOLA shot point. Early in mapping the HGA was fixed in its stowed position or constrained by gimbal stops, preventing concurrent nadir observations, but exit occultations in the south corresponded to regions where heavy clouds were observed on preceding orbits.

Figures 12a,b show selected profiles of temperature vs. elevation above ground from southern early- and mid-winter during Year One. The temperature T_s at which solid CO_2 is in equilibrium with vapor at ambient pressure is shown as a dashed line. Surface pressure was ~ 400 Pa at elevations 2 km above datum, with $T_s = \sim 145$ K. Temperatures below T_s were seen as early as $L_s=110^\circ$ at 75°S , and continued at least until $L_s=161^\circ$ at 67°S , the latest time for which occultations were available. As southern winter progressed, the occultation geometry switched to daylight. Temperatures as low as 4 K below T_s were observed in late winter, despite sun angles as high as 10° above the horizon.

Figures 12c,d show northern winter examples, at ~ 1000 Pa and -4 km elevation. Temperatures below T_s were seen as early as $L_s=266^\circ$ at 55°N , and continued intermittently

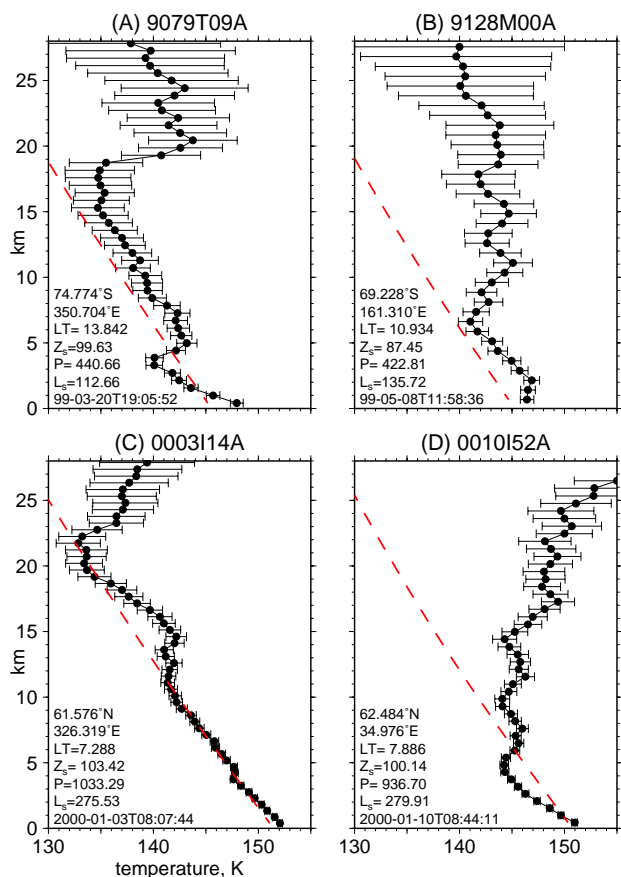


Figure 12. Winter temperature - elevation profiles from MGS Radio Science data: a) South Polar night; b) South Polar dawn; c) North Polar night; d) North Polar night. Error bars give $1\text{-}\sigma$ uncertainty in temperature. Dashes show CO_2 saturation temperature at ambient pressure from *James et al.* [1992].

at least until $L_s=297^\circ$ at 63°N . These occurrences of cold temperatures in both hemispheres lie inside the regions of reflective clouds shown in Plate 1.

Subpolar thermal structure is temporally and spatially variable. In most profiles, temperatures decrease linearly up to a variable height, roughly 3 to 18 km, then rise in the middle atmosphere. Near-surface temperatures are buffered by surface CO_2 ice, hovering near CO_2 saturation with a lapse rate of 0.85 K km^{-1} . Examples (a) and (d) show intervals with more rapid cooling within the first 3 km, closer to the dry adiabatic lapse rate of $4.3^\circ\text{ K km}^{-1}$ [Pettengill and Ford, 2000]. Adiabatic ascent quickly drives CO_2 into supersaturation.

Hinson and Wilson [2002] have interpreted the atmospheric structure during southern midwinter ($L_s=134\text{-}148$)

arising from transient eddies and stationary waves. Such disturbances cause temperatures to vary by as much as $\sim 15\text{ K}$ at a given altitude, latitude and time. The coldest regions occur within 5 km of the ground at longitudes near 330°E , where the intensity of cloud activity peaks (Figure 5b). Temperature inversions as seen in Figure 12a in the early southern winter imply either phase disequilibrium or local depletion of CO_2 . Disequilibrium may easily occur, since nucleation of CO_2 crystals requires at least $\sim 2\text{ K}$ supercooling [Colaprete and Toon, 2002; Glandorf et al., 2002]. Once condensation is initiated, clouds would quickly restore equilibrium by releasing latent heat and lowering CO_2 partial pressure. CO_2 depletion is likely to be short-lived in view of the vigorous mixing of the winter polar atmosphere. Temperature profiles (Figure 12b) later in the season and further toward the equator, where little cloud activity occurred, hover just above the equilibrium temperature. In midwinter profiles ($L_s=135^\circ$), the supercooled region is generally $< 6\text{ km}$ above the surface, but occasionally a high inversion develops at 15-20 km in late winter, as late as $L_s=159^\circ$. Such elevations normally lie beyond the 10-km-high range gate of MOLA, but clouds are occasionally detected there.

Northern winter profiles (Figures 12c and d) during January 2000 at $61\text{-}63^\circ\text{N}$ show comparable thermodynamic relationships in early winter ($L_s=275\text{-}297^\circ$). Temperatures are low enough to condense CO_2 at heights up to 22 km above ground, but more typically 0-5 km. The vertical extent of the region that follows the saturation curve varies markedly, as was seen in the south the previous year. On days where cold temperatures persist to high elevations, comparatively higher cloud fronts are observed by MOLA.

Profiles (b) and (d) (Figure 12) exhibit marked vertical wave structure. Such waves can give rise to multiple layers of clouds. Figure 13 shows 5 separate layers of clouds, spaced 1.5 - 3 km apart.

7. Cloud Return Characteristics

Terrestrial clouds, such as those observed by the SLA instrument, have finite thickness and extended waveforms, corresponding to cloud fronts of fairly uniform particle density and optical attenuation. MOLA did not have the power or data bandwidth to return a digitized waveform, but provided some ability to discriminate cloud types via separate filter channels (Table 1) and measurements of pulse width and energy at the detector threshold. The backscatter cross-section of a cloud within a MOLA footprint, multiplied by the two-way path attenuation through the medium [Spinhirne et al., 1989], yields a signal of variable intensity and duration, from which information about particle distribution and vertical extent may be inferred. A full analysis of

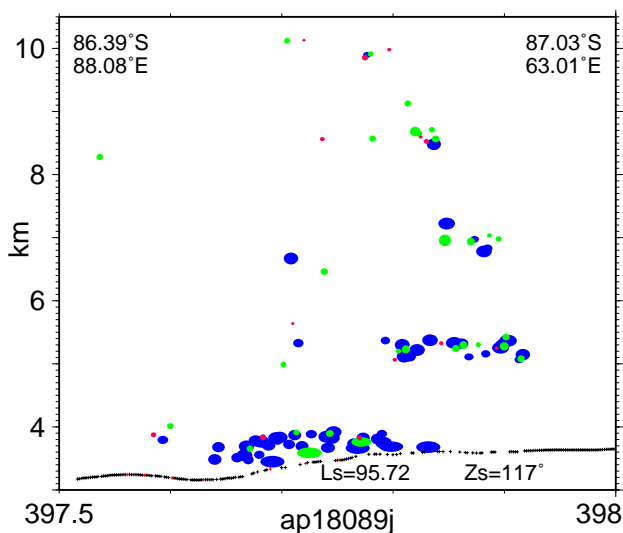


Figure 13. Multiple cloud decks over the south pole. The vertical exaggeration is 10:1.

cloud backscatter and extinction is underway and lies beyond the scope of this work, but the unusually brief and strong backscatter of southern circumpolar clouds merits some discussion.

Ground returns from the smooth, bright polar regions occur exclusively on channels 1 and 2, exhibiting relatively short pulse widths and high signal, usually saturating the detector. Cloud returns occur on all four channels, and the majority are unsaturated. Those that are saturated are usually within 200 m of the ground, as in Figure 7. Forward scattering close to ground may strengthen cloud returns, but saturated cloud returns mainly appear to be triggered by near-surface layers distinct from ground. The majority of energy and pulse width counts for elevated cloud returns are unsaturated.

Figures 14 show the occurrence of unsaturated cloud energies and pulse widths on each channel as density plots. The coordinates are raw energy (Pulse Energy, 0-255) and width (PW, 0-63) counts output by MOLA. Counts can be scaled to Volt-seconds and seconds as in *Abshire et al.* [2000]. Monitored via an internal source, these measurements are stable but their calibration at small values is affected by nonlinear response of the detector. As explained below, we may instead compare them to contours of constant ratio of mean voltage to threshold, using nominal calibration factors.

The raw MOLA measurements are affected by laser output, threshold settings and system noise. Even in the absence of noise, the full pulse width and energy cannot be

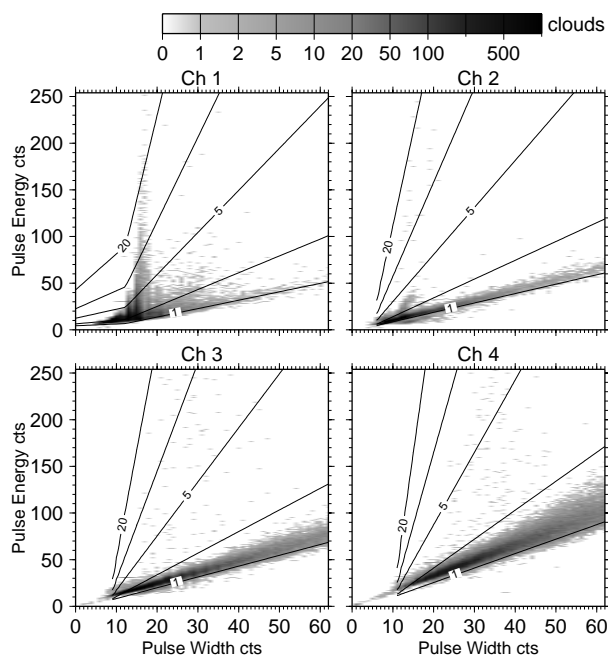


Figure 14. Frequency plots of MOLA energy and pulse width counts for cloud returns on channels 1-4 at latitudes south of 50°S during southern winter. Contours of z (defined in text) show average pulse height relative to detector threshold level. Z values are contoured at 1, 2, 5, 10, and 20 times typical nighttime threshold.

determined uniquely using the two measurements available without assuming a model waveform. Such waveforms are unknown for Martian clouds, but one can compare pulses in a relative fashion. The signal received during the interval exceeding threshold is integrated over the pulse width. For most clouds, the average signal is not much greater than the threshold voltage itself, and the energy is roughly proportional to the pulse width. Such clouds form an array bounded by a minimum energy line. For a few clouds, signal is many times the detection threshold. We quantify this with the parameter [*Abshire et al.*, 2000]

$$z = \frac{A_y}{yW_y} \quad (3)$$

where W_y is the pulse width between threshold crossings, and A_y is the detector signal integrated while voltage exceeds y .

Weak returns typically have $z < 1.5$, while the strong channel 1 and 2 returns have $z > 2$ (Figure 14). In the south circumpolar clouds, two arrays of cloud returns are evident: high-energy returns with relatively short pulse width (high z), and returns with variable energies and longer pulse

widths (low z). The bimodal distribution is only apparent for the clouds on channels 1 and 2. The arrays of high z returns occur preferentially at circumpolar latitudes [Ivanov and Muhleman, 2001]. The energy and pulse widths of clouds in Figure 7 lie mainly in the high- z array. The modal pulse width of the channel 1 high- z clouds is ~ 30 ns.

Channel 3 and 4 returns typically have long times above threshold, 500-1000 ns, and therefore relatively high total energy with modest backscatter in a given distance. Channel 1 and 2 clouds in the south circumpolar belt generally have times < 60 ns, considerably shorter than that of terrestrial clouds. Such short times are not well resolved due to the filter applied to the detector output, but the backscatter cross-section of these clouds is necessarily very high since all triggering photons are returned within a 3-9 m distance. Total energy return of the circumpolar clouds is typically 0.5-5% of a perfect Lambertian reflector, and often higher within ~ 200 m of ground.

The limited information and dynamic range in a single MOLA shot cannot fully characterize even first-return cloud waveforms, but the preponderance of either ground returns or channel 1 cloud returns in Year 1 to the exclusion of higher channels (Figure 7) and the similarly homogeneous region of channel 2 returns in Figure 8 argues for a distinct type of clouds, whose waveform peak is narrower than 60 ns.

Another distinctive feature of the "channel 1 clouds" is that almost invariably, ground returns adjacent to the clouds are saturated, typically at energies of 11-20%. Since reflectivity r_s is unlikely to be more than 45%, less than half the photons have been absorbed in each direction. The total opacity $\tau < 0.7$ for all cloud fronts traversed by a ground shot, including atmospheric haze, and the extinction of an individual cloud must be considerably less.

8. Discussion

MOLA was designed to sense weak cloud reflections from particles extended over 80+ meters of height. Had clouds only triggered on channel 4, we would have seen something of the dust cycle and the CO₂ precipitation process. Favorable geometry and instrument performance provided more sensitive aerosol detection than anticipated, including the completely unforeseen detection of cloud fronts only a few meters thick.

The channel 1 and 2 clouds are dispersed over several km height. At times they comprise up to one third of the MOLA returns in a given packet, but seldom form a coherent layer [Ivanov and Muhleman, 2001]. These cloud fronts are not dispersed at lower concentrations in thicker layers or they would trigger over the integration times of channels 3 and 4,

resulting in a mixture of channels. The vertical distribution of these triggers could be created by many separate cloud sheets descending to the ground. Since MOLA can record only the first trigger above threshold, a given shot may have encountered more than one such layer. If their distribution were random it is likely that several layers would be traversed along the light path to ground. Such layers would necessarily be very transparent.

The strong backscatter of the channel 1 and 2 clouds could instead result from thin sheets of crystalline flakes subparallel to the ground, whose reflections at zero phase and zero incidence are detected over brief intervals of time. Specular reflections of sunlight are commonly observed from airplanes in the terrestrial winter skies from oriented ice crystals. Either specular reflection or zero-phase reflection would suffice to make ice visible to MOLA. Channel 1 returns were not seen during offnadir passes, but strong cloud returns on channels 2-4 were obtained during 21° offnadir passes over the south pole at $L_s=104^\circ$ in Year 2. No such passes took place prior to raising the channel 1 threshold in Year 1, so it is impossible to say whether nadir geometry is required to see channel 1 clouds.

Another possibility is that the channel 1/2 returns are not clouds at all, but specular reflections from individual snowflakes! Single flakes would produce very short pulse widths, and explain the diffuse vertical and lateral distribution of returns. A link analysis shows that large crystals are detectable. A sparse (\sim one per cubic meter), randomly oriented population of centimeter-sized flakes would occasionally orient a crystal face normal to the incident laser beam, but otherwise produce minimal attenuation. A 45 mJ pulse, a Gaussian beam pattern with divergence $\gamma = 92.5 \mu\text{rad}$ [Abshire et al., 2000], at periapse range $z_{\text{Mars}} = 370$ km, has intensity of $\sim 6.1 \mu\text{J m}^{-2}$ at its center. A circular area of 1 cm diameter would receive 480 pJ. Assuming the same divergence, total reflection back to the 0.5-m MOLA telescope would provide an energy of 12.5 fJ, in a return pulse as brief as the outgoing pulse. This is ~ 600 times the energy of a typical channel 1/2 cloud. With an index of refraction of about 1.4, CO₂ crystals would reflect about 3% of incident light at entering and exiting planar faces, leaving about 36-fold margin for detection. If the optical divergence of reflections from smooth faces were no more than six times greater than that of the incoming beam, occasional large, favorably oriented crystals could appear as channel 1/2 clouds. Such particles would have to be thin so as to remain suspended long enough to achieve adequate dimensions. The latent heat of crystallization would keep their concentration low, leading to minimal attenuation of ground returns and few returns on higher channels.

The gap between the south polar clouds and the circum-

polar belt may mark the limit of winter storms. There is a similar but less pronounced gap in the north. Temperatures in the polar night often dip below that of dry ice, but clouds may not form spontaneously until triggered by some stimulus. The injection of CO₂ enriched atmosphere [Kieffer *et al.*, 1977], dust particles, or even water ice on the edges of the polar cap could lead to rapid condensation of CO₂. Such mechanisms would tend to precipitate out particles, creating a region of low cloud density nearer the pole. Alternatively, condensation may be triggered simply by supercooling, and the dynamics of the polar vortex may isolate the circumpolar band from the polar clouds.

The properties of CO₂ snow under Martian conditions have only recently been studied [Forget *et al.*, 1995; Foster *et al.*, 1998]. Daylight warms the upper atmosphere as it reaches polar regions, but clouds affect radiative transport and may allow temperatures close to the surface to remain in equilibrium with dry ice. At least some regions of the south polar cap with very low thermal brightness temperatures are associated with clouds [Titus *et al.*, 2001]. Radio occultations are sparsely distributed with season and latitude, but where available, indicate that the dense nocturnal clouds at both poles are closely associated with a region of super-saturated CO₂. The occasional reflective ground clouds at mid-latitudes may reveal nocturnal condensation of volatiles from the sublimating seasonal cap. Condensation at mid-latitudes is almost certain to be some form of water ice. Interaction with dust is probably involved, since they are surrounded by absorptive clouds.

Absorptive clouds clearly mark the advance of the northern seasonal cap, and the recession of both caps. The clouds in Plate 2 show MOLA's detection not only of major dust storms such as that beginning at $L_s=220^\circ$ in the north, but earlier ones at $L_s=140^\circ$ and 160° also detected by TES [Smith *et al.*, 2001c]. Winds could be excited by the albedo contrast across this boundary. Such strong winds would suffice to stir up dust. MOLA has also seen dust devils occurring prior to the development of a major storm, in Year 2. It is not clear whether either of these phenomena is responsible for the onset of global storms, but they are temporally related. Monitoring of the effects of dust at the 1064-nm wavelength of MOLA are ongoing.

Water is a scarce commodity in the Martian atmosphere, but may at times achieve significant concentrations due to sublimation. We have no direct evidence for reflections from water ice, but these would be most likely to occur at night, when temperatures are conducive to frost. Extreme cold would likely remove most of the water, but in more temperate conditions along the edges of the seasonal caps we see absorptive clouds that become visible in their interiors as low ground fogs. Although seen in twilight, none of the

low, dense, nonpolar clouds occurred in the afternoon local time. We speculate that these are dust clouds revealed by a reflective diurnal coating of H₂O ice.

9. Conclusions

The MOLA instrument has generated more than half a million atmospheric lidar observations. As an active instrument, it is uniquely suited to both daytime and nighttime observations of clouds. While cloud reflections are mainly seen at night, some types of clouds are visible in daylight, particularly dust devils. It is very probable that water ice is also detected, as concentrated bright ground fogs coating dust, and as a dispersed attenuation over major volcanoes.

The atmosphere from ground to 20 km height has active, highly variable processes that intermittently produce clouds. We have identified reflective and absorptive clouds in an automated fashion. MOLA has mapped the densities of such clouds with respect to season and location, over a period spanning two Martian years. Our observations suggest that cloud cover was less during the second year at both poles.

Radio Science observations confirm that dry ice precipitation generates polar winter clouds in the lower atmosphere. Cloud density in the south polar winter is controlled by stationary and transient atmospheric disturbances, and possibly by circumpolar storms. Cloud measurements provide a window into the changing climate of the red planet, and have generated some puzzling findings as well. The south polar winter clouds are most peculiar, and may actually be single large snowflakes.

Acknowledgments. The MOLA investigation is supported by the NASA Mars Exploration Program. We recognize contributions from J. B. Abshire, R. Afzal, J. B. Blair, P. Ford, D. Muhleman, G. Pettengill, X. Sun and the entire MOLA instrument and operations team. A. Ivanov provided assistance at all stages, and provided manuscripts in advance of publication. D. Hinson and an anonymous reviewer provided thorough reviews. We appreciate the work of the MGS Radio Science Team for diligently monitoring signals at all hours to provide superb quality data. The Generic Mapping Tools software [Wessel and Smith, 1998] facilitated the analysis.

References

- Abshire, J. B., X. Sun, and R. S. Afzal, Mars Orbiter Laser Altimeter: Receiver model and performance analysis, *Appl. Opt.*, 39, 2440–2460, 2000.
- Banerdt, W. B., and G. A. Neumann, The topography (and ephemeris) of Phobos from MOLA ranging, *Lunar Planet. Sci. Conf.*, XXX, 1999.
- Bufton, J. L., J. B. Blair, J. Cavanaugh, J. B. Garvin, D. Harding, D. Hopf, K. Kirks, D. Rabine, and N. Walsh, Shuttle laser al-

- timer (SLA), in *Proc. Shuttle Small Payloads Symp.*, vol. CR-3310, pp. 83–91, NASA, Greenbelt, MD, 1995.
- Cantor, B. A., P. B. James, M. Caplinger, and M. J. Wolff, Martian dust storms: 1999 Mars Orbiter Camera observations, *J. Geophys. Res.*, *106*, 23,653–23,687, 2001.
- Chamberlain, T. E., H. L. Cole, R. G. Dutton, G. C. Greene, and J. E. Tillman, Atmospheric measurements on Mars: The Viking meteorology experiment, *Bull. Amer. Meteorol. Soc.*, *57*, 1094–1104, 1976.
- Colaprete, A., and O. B. Toon, Carbon dioxide clouds at high altitude in the tropics and in an early dense Martian atmosphere, *Icarus*, p. in press, 2002.
- Cole, T. D., M. T. Boies, A. F. C. A. S. El-Dinary, M. T. Zuber, and D. E. Smith, The Near Earth Asteroid Rendezvous laser altimeter, *Space Sci. Rev.*, *82*, 217–253, 1997.
- Forget, F., G. B. Hansen, and J. B. Pollack, Low brightness temperatures of Martian polar caps: CO₂ clouds or low surface emissivity?, *J. Geophys. Res.*, *100*, 21,219–21,234, 1995.
- Foster, J. L., A. T. C. Chang, D. K. Hall, W. P. Wergin, E. F. Erbe, and J. Barton, Carbon dioxide crystals: An examination of their size, shape, and scattering properties at 37 GHz and comparisons with water ice (snow) measurements, *J. Geophys. Res.*, *103*, 25,839–25,850, 1998.
- Garvin, J. B., J. L. Bufton, J. B. Blair, D. Harding, S. B. Luthcke, J. J. Frawley, and D. D. Rowlands, Observations of the Earth's topography from the Shuttle Laser Altimeter (SLA): Laser pulse echo recovery measurements of terrestrial surfaces, *Phys. Chem. Earth*, *23*, 1053–1068, 1998.
- Glandorf, D. L., A. Colaprete, M. A. Tolbert, and O. B. Toon, CO₂ snow on Mars and early Earth: Experimental constraints, *Icarus*, p. in press, 2002.
- Hansen, G. B., Control of the radiative behavior of the Martian polar caps by surface CO₂ ice: Evidence from Mars Global Surveyor measurements, *J. Geophys. Res.*, *104*, 16,471–16,486, 1999.
- Herr, K., and G. Pimental, Evidence for solid carbon dioxide in the upper atmosphere of Mars, *Science*, *167*, 47–49, 1970.
- Hess, S. L., R. M. Henry, and J. E. Tillman, The seasonal variation of atmospheric pressure on Mars as affected by the south polar cap, *J. Geophys. Res.*, *84*, 2923–2927, 1979.
- Hinson, D. P., and R. J. Wilson, Transient eddies in the southern hemisphere of Mars, *Geophys. Res. Lett.*, *29*(7), 10.1029/2001GL014,103, 2002.
- Hinson, D. P., R. A. Simpson, J. D. Twicken, and G. L. Tyler, Initial results from radio occultation measurements with Mars Global Surveyor, *J. Geophys. Res.*, *104*, 26,997–27,012, 1999.
- Hinson, D. P., G. L. Tyler, J. L. Hollingsworth, and R. J. Wilson, Radio occultation measurements of forced atmospheric waves on Mars, *J. Geophys. Res.*, *106*, 1463–1480, 2001.
- Ivanov, A. B., Some aspects of the Martian climate from the Mars Orbiter Laser Altimeter Investigation, Ph.D. thesis, California Institute of Technology, Pasadena, 2000.
- Ivanov, A. B., and D. O. Muhleman, Opacity of the Martian atmosphere from Mars Orbiter Laser Altimeter (MOLA) observations, *Geophys. Res. Lett.*, *25*, 4417–4420, 1998.
- Ivanov, A. B., and D. O. Muhleman, The role of sublimation for the formation of the northern ice cap: Results from the Mars Orbiter Laser Altimeter, *Icarus*, *144*, 436–448, 2000a.
- Ivanov, A. B., and D. O. Muhleman, Observations of the reflectivity of the Martian surface in the Mars Orbiter Laser Altimeter, *Lunar Planet. Sci. Conf.*, XXXI, 2000b.
- Ivanov, A. B., and D. O. Muhleman, Cloud reflection observations: Results from the Mars Orbiter Laser Altimeter (MOLA), *Icarus*, *154*, 190–206, 2001.
- Ivanov, A. B., G. A. Neumann, and D. O. Muhleman, Joint analysis of the MOLA radiometry data and TES Lambert albedo, *Eos Trans. AGU*, *82* (47), Fall Meet. Suppl., 2001.
- James, P. B., H. H. Kieffer, and D. A. Paige, The seasonal cycle of carbon dioxide on Mars, in *Mars*, edited by H. H. Kieffer, B. M. Jakosky, C. W. Snyder, and M. S. Matthews, pp. 934–968, Univ. of Ariz. Press, Tucson, 1992.
- James, P. B., B. A. Cantor, and S. Davis, Mars Orbiter Camera observations of the Martian south polar cap in 1999–2000, *J. Geophys. Res.*, *106*, 23,635–23,652, 2001.
- Kahn, R. A., The spatial and seasonal distribution of Martian clouds, and some meteorological implications, *J. Geophys. Res.*, *89*, 6671–6688, 1984.
- Kieffer, H. H., T. Z. Martin, A. R. Peterfreund, B. M. Jakosky, E. M. Miner, and F. D. Palluconi, Thermal and albedo mapping of Mars during the Viking primary mission, *J. Geophys. Res.*, *12*, 4249–4291, 1977.
- Kieffer, H. H., T. N. Titus, K. F. Mullins, and P. R. Christensen, Mars south polar spring and summer behavior observed by TES: Seasonal cap evolution controlled by frost grain size, *J. Geophys. Res.*, *105*, 9653–9699, 2000.
- Lindal, G. F., H. B. Hotz, D. N. Sweetnam, Z. Shippony, J. P. Brenkle, G. V. Hartsell, R. T. Spear, and W. H. J. Michael, Viking radio occultation measurements of the atmosphere and topography of Mars: Data acquired during 1 Martian year of tracking, *J. Geophys. Res.*, *84*, 8443–8456, 1979.
- Martin, L. J., P. B. James, A. Dollfus, K. Iwasaki, and J. D. Beish, Telescopic observations: Visual, photographic, polarimetric, in *Mars*, edited by H. H. Kieffer, B. M. Jakosky, C. W. Snyder, and M. S. Matthews, pp. 34–70, Univ. of Ariz. Press, Tucson, 1992.
- McGarry, J. F., L. K. Pacini, J. B. Abshire, and J. B. Blair, Design and performance of an autonomous tracking for the Mars Observer Laser Altimeter, *Conf. Lasers Electro-Optics*, *10*, CThR27, 1991.
- Muhleman, D. O., and A. B. Ivanov, Evolution of the Mars northern ice cap and results from the Mars Orbiter Laser Altimeter (MOLA), in *First Int. Conf. on Mars Polar Exploration*, edited by S. Clifford, D. Fisher, and J. Rice, pp. 28–29, Lunar Planet. Inst., Camp Allen, TX, 1998.
- Nozette, S., et al., The Clementine mission to the moon: Scientific overview, *Science*, *266*, 1835–1839, 1994.
- Pearl, J. C., M. D. Smith, B. J. Conrath, J. L. Bandfield, and P. R. Christensen, Observations of Martian ice clouds by the Mars Global Surveyor Thermal Emission Spectrometer: The first Martian year, *J. Geophys. Res.*, *106*, 12,325–12,338, 2001.
- Pettengill, G. H., and P. G. Ford, Winter clouds over the north Martian polar cap, *Geophys. Res. Lett.*, *27*, 609–612, 2000.
- Smith, D. E., G. A. Neumann, P. G. Ford, R. E. Arvidson, E. A. Guinness, and S. Slavney, Mars Global Surveyor Laser Altimeter precision experiment data record, *Tech. Rep. MGS-M-MOLA-3-PEDR-LIA-VI.0*, NASA Planetary Data System, 1999a.

- Smith, D. E., M. T. Zuber, R. M. Haberle, D. D. Rowlands, and J. R. Murphy, The Mars seasonal CO₂ cycle and the time variation of the gravity field: A General Circulation Model simulation, *J. Geophys. Res.*, *104*, 1885–1896, 1999b.
- Smith, D. E., M. T. Zuber, and G. A. Neumann, Seasonal variations of snow depth on Mars, *Science*, *294*, 2141–2146, 2001a.
- Smith, D. E., et al., Mars Orbiter Laser Altimeter: Experiment summary after the first year of global mapping of Mars, *J. Geophys. Res.*, *106*, 23,689–23,722, 2001b.
- Smith, M. D., J. C. Pearl, B. J. Conrath, and P. R. Christensen, Mars Global Surveyor Thermal Emission Spectrometer (TES) observations of dust opacity during aerobraking and science phasing, *J. Geophys. Res.*, *105*, 9539–9552, 2000.
- Smith, M. D., J. C. Pearl, B. J. Conrath, and P. R. Christensen, Thermal Emission Spectrometer results: Mars atmospheric thermal structure and aerosol distribution, *J. Geophys. Res.*, *106*, 23,929–23,945, 2001c.
- Smith, P. H., and M. Lemmon, Opacity of the Martian atmosphere measured by the Imager for Mars Pathfinder, *J. Geophys. Res.*, *104*, 8975–8985, 1994.
- Spinhirne, J. D., R. Boers, and W. D. Hart, Cloud top liquid water from lidar observations of marine stratocumulus, *J. Appl. Meteorology*, *28*, 81–90, 1989.
- Sun, X., J. B. Abshire, G. A. Neumann, and M. Zuber, Radiometry measurements of Mars at 1064 nm using the Mars Orbiter Laser Altimeter, *Eos Trans. AGU*, *82* (47), *Fall Meet. Suppl.*, 2001.
- Tamppari, L. K., R. W. Zurek, and D. A. Paige, Viking era water ice clouds, *J. Geophys. Res.*, *105*, 4087–4107, 2000.
- Titov, D. V., W. J. Markiewicz, N. Thomas, H. U. Keller, R. M. Sablotny, M. Tomasko, M. T. Lemmon, and P. H. Smith, Measurements of the atmospheric water vapor on Mars by the Imager for Mars Pathfinder, *J. Geophys. Res.*, *104*, 90,191–90,206, 1999.
- Titus, T. N., H. H. Kieffer, K. F. Mullins, and P. R. Christensen, TES pre-mapping data: Slab ice and snow flurries in the Martian north polar night, *J. Geophys. Res.*, *106*, 23,181–23,196, 2001.
- Tyler, G. L., G. Balmino, D. P. Hinson, W. L. Sjogren, D. E. Smith, R. A. Simpson, S. W. Asmar, P. Priest, and J. D. Twicken, Radio science observations with Mars Global Surveyor: Orbit insertion through one year in mapping orbit, *J. Geophys. Res.*, *106*, 23,327–23,348, 2001.
- Tyler, G. L., et al., Radio science investigations with Mars Observer, *J. Geophys. Res.*, *97*, 7759–7779, 1992.
- Wang, H., and A. P. Ingersoll, North polar cloud activity on Mars from mid summer to late fall, *LPSC*, *XXXII*, 1460, 2001.
- Wessel, P., and W. H. F. Smith, New, improved version of Generic Mapping Tools released, *Eos Trans. AGU*, *79*, 579, 1998.
- Zuber, M. T., D. E. Smith, S. C. Solomon, D. O. Muhleman, J. W. Head, J. B. Garvin, J. B. Abshire, and J. L. Bufton, The Mars Observer Laser Altimeter investigation, *J. Geophys. Res.*, *97*, 7781–7797, 1992.
- Zuber, M. T., D. E. Smith, A. F. Cheng, and T. D. Cole, The NEAR laser ranging investigation, *J. Geophys. Res.*, *102*, 23,761–23,773, 1997.
- Zuber, M. T., et al., Observations of the north polar region of Mars from the Mars Orbiter Laser Altimeter, *Science*, *282*, 2053–2060, 1998.
- Zurek, R. W., J. R. Barnes, R. M. Haberle, J. B. Pollack, J. E. Tillman, and C. B. Leovy, Dynamics of the atmosphere of Mars, in *Mars*, edited by H. H. Kieffer, B. M. Jakosky, C. W. Snyder, and M. S. Matthews, pp. 835–933, Univ. of Ariz. Press, Tucson, 1992.
- G. A. Neumann, D. E. Smith, Laboratory for Terrestrial Physics, Code 920, NASA/Goddard Space Flight Center, Greenbelt, MD 20771 (e-mail: neumann@tharsis.gsfc.nasa.gov)
- M. T. Zuber, Department of Earth, Atmospheric and Planetary Sciences, Massachusetts Institute of Technology, 54-518, Cambridge, MA 02139-4307

Received January 24, 2002; revised May 9, 2002; accepted May 21, 2002.